Energy 344 (2026) 140013

Contents lists available at ScienceDirect

Energy

journal homepage: www.elsevier.com/locate/energy

Fracture susceptibility and depressurization dynamics in CO_2 pipelines under uncertainty

Gabriele Bicelli [a], Giulia Libero [b], Davide Picchi [a,*], Valentina Ciriello [b]

[a] Department of Mechanical and Industrial Engineering, Università degli Studi di Brescia, Brescia 25123, Italy
[b] Department of Civil, Chemical, Environmental, and Materials Engineering, University of Bologna, Bologna 40136, Italy

ARTICLE INFO

Keywords:
Carbon dioxide transport
Homogeneous equilibrium model
Polynomial chaos expansions
Uncertainty quantification

ABSTRACT

Since the success of large-scale carbon capture and storage (CCS) infrastructures relies on the safety of pressurized CO_2 pipelines, quantifying the susceptibility to running ductile fracture during planned or accidental depressurization is still a key challenge in the field. In this work, we present an integrated framework for uncertainty quantification in CO_2 pipelines that combines a high-fidelity, one-dimensional transient solver based on the Homogeneous Equilibrium Model with a reduced-order surrogate constructed via Polynomial Chaos Expansion. The methodology is applied to two representative infrastructures, the Cortez and Weyburn pipelines, to analyze fracture-related metrics based on the Battelle Two-Curves Method and the depressurization dynamics under uncertainty in operating conditions typical of CO_2 transport. Our analysis reveals that the pipe diameter (and its thickness) and the initial temperature are the main parameters in determining the pipe vulnerability to the running ductile fracture rather than the initial pressure. Specifically, only if the initial temperature is below a certain value (that depends on the pipeline), the onset of the fracture is prevented. In addition, we show that the minimal temperature reached during the depressurization has a similar behavior, while the discharged mass, relevant in the case of leaks, depends on both the initial temperature and pressure. Overall, the proposed approach achieves high predictive accuracy while drastically reducing computational cost, providing a basis for risk assessment to support safer and more robust CCS pipeline design and operation.

1. Introduction

According to the IEA Net Zero Roadmap [1], in order to contain climate change and keep the global temperature rise within 1.5°C by 2100, it is desired to cut the anthropogenic CO_2 emissions. This ambitious target requires a wide range of measures, among which a key role is represented by Carbon Capture and Storage (CCS), namely a combination of technologies to capture and store, or re-utilize about 1.2 Gt/year of carbon dioxide by 2030 and 8 Gt/year by 2050. In the near future the success of CCS relies on a vast and efficient network of pipelines to transport the captured CO_2 to storage sites (see e.g., [2–5]), but, unfortunately, except for the enhanced oil recovery operations [6], transporting carbon dioxide over long distances is still an object of industrial and academic research due to its unique characteristics compared to natural gas.

One of the primary concerns in expanding such infrastructure is represented by its efficiency and safety, especially if the pipelines are placed close to urban or densely populated areas where hazardous CO_2 concentrations must be avoided [7]. Unlike natural gas, carbon dioxide is transported in a highly-pressure dense-liquid state [8] leading to potentially dangerous scenarios. In case of planned or accidental depressurization, in fact, a sudden drop in temperature and pressure can lead to pipe fractures (e.g., running ductile fractures — RDF) and leakage into the environment [9–11]. Specifically, RDF is a well-known issue associated with pressurized pipelines where an accidental puncture or corrosion crack propagates along the pipe (up to several meters) driven by the decompression wave and the energy released by the escaping fluid. A single running ductile fracture can lead to a catastrophic failure of the pipeline, and tons of carbon dioxide may be released into the environment in a very short amount of time. So far, the common strategies to deal with RDF control rely on the classical Battelle Two-Curve method (BTCM) [12] adapted to the specificity of CO_2 transport [13,14].

In recent decades, the common approach is to study the depressurization problem from a deterministic point of view. Up to now, only few

* Corresponding author.
E-mail addresses: davide.picchi@unibs.it (D. Picchi), v.ciriello@unibo.it (V. Ciriello).

https://doi.org/10.1016/j.energy.2026.140013
Received 9 October 2025; Received in revised form 23 December 2025; Accepted 11 January 2026
Available online 13 January 2026

experiments have been conducted to study the dynamics of depressurization and fracture propagation both in laboratory-scale or real-scale setups (see for example, [11,15–18]) while many modeling approaches have been proposed ranging from the simplest Homogeneous Equilibrium Model (HEM) [9,19–22], to the drift-flux model [23,24], or the more complex and computational demanding two-fluids model [25–28]. In practical applications, however, a great level of uncertainty is present due the variability of the operating conditions (e.g., initial pressure and temperature). This implies that, when used in real scenarios, the computational costs of such models become prohibitive, preventing a systematic quantification of the pipeline susceptibility to running ductile fracture.

To fill this gap, we present an integrated approach to quantitative risk assessment for CO_2 depressurization scenarios coupling an in-house one-dimensional, transient, multiphase solver based on the HEM with a polynomial chaos expansion (PCE) reduced-order model for fast analysis (e.g., [29–31]). The PCE offers an efficient model-reduction strategy for approximating the response surface of quantities of interest across the variability range of selected governing parameters, requiring only a limited number of high-fidelity simulations. This approximation takes the form of a polynomial series whose computational cost is negligible compared to that of high-fidelity simulations (the HEM model in our case), enabling extensive ensemble-based investigations such as global sensitivity analysis and uncertainty quantification. These capabilities make PCE a valuable alternative to conventional Monte Carlo techniques [32,33] and a useful tool for experiment interpretation and design [22]. The computational advantage, however, is maintained only when the number of uncertain parameters is small. PCE scales poorly with dimensionality, and its efficiency deteriorates rapidly as the number of random inputs increases. For high-dimensional input spaces, alternative surrogate approaches — such as neural networks combined with cost-reduction strategies for training-data generation — can be more suitable [34].

In the present study, the limited number of uncertain inputs preserves the computational effectiveness of PCE. As a result, the method delivers substantial computational savings while providing a straightforward and accurate approximation of the input–output relationships relevant to the case study. We demonstrate that this approach significantly lowers computational cost while retaining accuracy, combining the fidelity of high-resolution simulations with the efficiency of reduced-order models. Specifically, we derive approximations of the response surfaces of the metrics describing the susceptibility of CO_2 pipelines to RDF and transient flow behavior, in the space of variability of the initial operating temperature and pressure. Then, the high computational efficiency of the resulting surrogates enables global sensitivity analysis (GSA) that would be impractical with existing high-fidelity models. Overall, the PCE surrogates support efficient prediction and assessment of how variability in governing parameters influences the quantities of interest, providing insights essential for safe and economically viable pipeline design and operation.

The paper is organized as follows. In Section 2 the homogeneous equilibrium model governing equations and closure relations are presented. In Section 3 the numerical methods implemented for the problem resolution are briefly described, as well as the model validation against experimental data from [11] while the grid-convergence test to assess numerical accuracy is given in Appendix B. In Section 4 a focus is given on Running Ductile Fracture and depressurization phenomena, while Section 5 is devoted to the description of the surrogate models. In Section 6 results are reported and discussed, and finally, Section 7 concludes the paper.

2. Homogeneous equilibrium model

2.1. Governing equations

In this work, we use the Homogeneous Equilibrium Model (see [35]) to simulate the depressurization of pure CO_2 in a horizontal tube as shown in Fig. 1. The HEM assumes local thermodynamic equilibrium and, since the length of the pipeline is much greater than its inner diameter ($L \gg D$), the quantities of interest are treated in terms of cross-section averaged mixture properties at both single-phase (gas or liquid) and two-phase (gas–liquid) conditions.

The balance of mass, momentum, and (total) energy for single-phase flow conditions are given by

$$\frac{\partial \rho}{\partial t} + \frac{\partial(\rho u)}{\partial x} = 0\,, \tag{1}$$

$$\frac{\partial(\rho u)}{\partial t} + \frac{\partial(\rho u^2 + p)}{\partial x} = G + f\,, \tag{2}$$

$$\frac{\partial E}{\partial t} + \frac{\partial((E+p)u)}{\partial x} = Q + Gu\,, \tag{3}$$

with ρ being the fluid density, u the fluid velocity in the x-direction, $E = \rho(e + \frac{1}{2}u^2)$ the total energy per unit volume, and p the pressure; the source terms on the r.h.s of Eqs. (2) and (3) are the gravitational body force, G, the friction with the pipe wall, f, and the heat exchanged between the fluid and the surrounding environment, Q. Among the available EoS for carbon dioxide, we use the Span and Wagner EoS [36] coupling the HEM with the open-source property calculator CoolProp [37] while the thermal conductivity, κ, and the dynamic viscosity, μ, are modeled as presented in [38,39], respectively. Since the HEM is written in conservative form in terms of density, momentum and total energy, the thermodynamic variables such as the pressure $p(\rho, E)$ are computed using the Equation of State (EoS) via flash calculations (see e.g. [40]); note that these routines are already implemented in CoolProp.

When the carbon dioxide is at two-phase flow conditions, the density and energy into Eqs. (1)–(3) are replaced by mixture quantities as

$$\rho = \left(\frac{\alpha}{\rho_g} + \frac{1-\alpha}{\rho_l}\right)^{-1} \qquad \text{and} \qquad e = e_g\alpha + e_l(1-\alpha)\,, \tag{4}$$

where α is the gas mass fraction, also referred as vapor quality, and the subscripts g and l stays for gas and liquid, respectively. The other properties, such as viscosity, thermal conductivity, and specific heat capacity are modeled similarly as in Eq. (4), through a weighted average based on the gas mass fraction as

$$\mu = \alpha\mu_g + (1-\alpha)\mu_l \quad \text{and} \quad \kappa = \alpha\kappa_g + (1-\alpha)\kappa_l \quad \text{and} \quad c_p = \alpha c_{p,g} + (1-\alpha)c_{p,l}\,. \tag{5}$$

2.2. Model closures

The speed of sound is a critical parameter in depressurization simulations, as it determines the propagation of pressure waves. When CO_2 is at single-phase flow conditions, we rely on the [36] EoS whose predictions of the speed of sound are accurate to within 1 percent of error. In the two-phase scenario, instead, the two-phase flow pattern affects the speed of sound for the mixture [41] and its definition is not unique. Specifically, under the typical assumptions behind the HEM (thermal equilibrium and homogeneous mixture), it can be derived analytically, leading to [25,42]:

$$c_{\text{HEM}} = \left[\rho\left(\frac{\alpha}{\rho_g c_g^2} + \frac{1-\alpha}{\rho_l c_l^2} + TC_{p,g}\left(\frac{\frac{1}{\rho_l}-\frac{1}{\rho_g}}{h_g - h_l} + \frac{\gamma_g}{\rho_g c_g^2}\right)^2 + TC_{p,\ell}\left(\frac{\frac{1}{\rho_l}-\frac{1}{\rho_g}}{h_g - h_l} - \frac{\gamma_l}{\rho_l c_l^2}\right)^2\right)\right]^{-1/2} \tag{6}$$

where

$$c_k = \left(\frac{\partial p_k}{\partial \rho_k}\right)_s\,, \qquad \gamma_k = \frac{1}{\rho_k}\left(\frac{\partial p_k}{\partial e_k}\right)_{\rho_k}\,, \qquad C_{p,k} = \alpha_k \rho_k c_{p,k}\,, \tag{7}$$

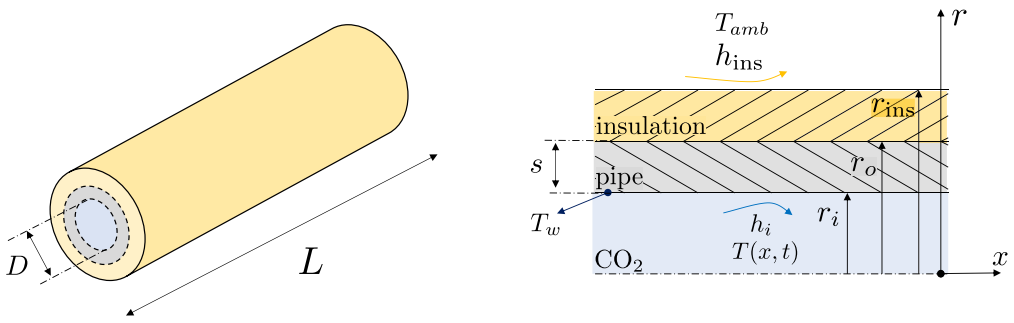

Fig. 1. Sketch of the insulated pipeline.

are the speed of sound, the Grüneisen parameter, and the extensive heat capacity, respectively, with the subscript $k = g, l$; $c_{p,k}$ is the specific heat capacity, with α_k the mass fraction and h_g and h_l are the gas and liquid enthalpy. Although formally correct, this formulation does not properly describe the evolution of the sound speed in the whole range of volume fractions, and, therefore, we replace it with the simplified Wood's correlation [43]. The latter is in good agreement with experimental observations in the whole range of volume fractions [41] and it is given by:

$$\frac{1}{\rho^2 c^2} = \frac{1-\alpha}{\rho_l^2 c_l^2} + \frac{\alpha}{\rho_g^2 c_g^2}. \tag{8}$$

The contribution of the wall friction is incorporated as a source term in the momentum equation, Eq. (2), and is modeled as

$$f = \frac{-f_c \dot{m}|\dot{m}|}{2\rho D}, \tag{9}$$

where $f_c = f(\text{Re})$ is the Darcy friction factor, which is a function of the Reynolds number $\text{Re} = \rho u D/\mu$, $\dot{m}$ is the mass flux. Here, the friction factor is obtained solving iteratively the Colebrook–White equation [44], being ε the pipe roughness.

$$\begin{cases} \frac{1}{\sqrt{f_c}} = -2.0 \log_{10}\left(\frac{\varepsilon/D}{3.7} + \frac{2.51}{\text{Re}\sqrt{f_c}}\right), & \text{for Re} \geq 2300 \\ f_c = \frac{64}{\text{Re}}, & \text{for Re} < 2300\,. \end{cases} \tag{10}$$

The body force term in Eq. (2) is given by $G = \rho g \sin(\theta)$ where θ is the pipe's inclination relative to the ground plane; in this work the pipe is assumed horizontal for the sake of simplicity.

In this work, we focus solely on the heat exchange between the fluid and the environment in the radial direction, neglecting axial conduction (the pipe length is much greater than its diameter and thickness), similarly to Munkejord and Hammer [19]. Therefore, we use Newton's law of convective cooling applied as a boundary condition between the outer surface of the pipeline and the environment, solving the heat equation in the radial direction as a two-layer conduction problem (the pipe and its insulation), as in Fig. 1,

$$\hat{\rho}(r)\hat{c}_p(r)\frac{\partial \hat{T}}{\partial t} = \frac{1}{r}\frac{\partial}{\partial r}\left(r\hat{\kappa}(r)\frac{\partial \hat{T}}{\partial r}\right) \qquad \text{with} \qquad r \in [r_i, r_{ins}], \tag{11}$$

where $\hat{\rho}(r)$, $\hat{c}_p(r)$ and $\hat{\kappa}(r)$ are density, the specific heat, and the thermal conductivity of the solids (i.e., the pipe and the insulation), respectively; the hat refers to the temperature in the solids and is used to distinguish the temperature in the solid with the one of the fluid. Then, once the temperature distribution is known, the heat transfer term Q in Eq. (3) is calculated as

$$Q = \frac{2h_i}{r_i}(T_w - T), \tag{12}$$

with $T_w = \hat{T}(r_i)$ and T being the wall and fluid temperatures, respectively, $r_i = D/2$ the inner radius of the pipe, and h_i the inner convective coefficient. The convective coefficient h_{ins} between the pipeline insulation and the environment at T_{amb}, is assumed equal to 4 W/m^2 K as in [11], while the inner convective coefficient h_i is calculated for single-phase flow conditions as

$$h_i = \frac{\text{Nu}\,\kappa}{D}, \tag{13}$$

where Nu is the Nusselt number, κ the thermal conductivity of the fluid, and D inner diameter of the pipe. The Nusselt number is estimated using the classical Dittus–Boelter correlation [45], valid for $0.6 \leq \text{Pr} \leq 160$

$$\begin{cases} \text{Nu} = 3.66, & \text{for Re} < 10000 \\ \text{Nu} = 0.023\text{Re}^{4/5}\,\text{Pr}^m, & \text{for Re} \geq 10000\,, \end{cases} \tag{14}$$

where $m = 0.3$ if the fluid is cooled or $m = 0.4$ if it is heated, Pr is the Prandtl number, defined as $\text{Pr} = \mu c_p/\kappa$ (recalling that in two-phase conditions we use the mixture properties to compute dimensionless numbers). When the carbon dioxide is at two-phase conditions, the single-phase convective coefficient, Eq. (13), is augmented following Kandlikar's [46] correlation.

2.3. Initial and boundary conditions

The governing equations Eqs. (1), (2), and (3) require an initial and boundary conditions. Specifically, the fluid is initialized at $t = 0$ s by imposing a uniform pressure p_0 and temperature T_0 in the entire domain, mimicking the conditions preceding a depressurization event. In the first cell, the incoming numerical flux is set equal to the outgoing flux corresponding to an infinite pipe boundary condition.

In this kind of simulations, the outlet boundary condition has a significant impact on the results, as the external pressure dictates both the propagation of the depressurization wave and the minimum temperatures reached near the pipe opening. Here, the outflow is modeled by imposing a state equal to that of the last computational cell, limiting the pressure to the critical pressure (assuming sonic chocking at the outlet, as long as it remains greater than ambient pressure, $p_{\text{amb}} = 101325$ Pa). Such critical pressure is derived under the assumption of steady-state choked flow, consistently with the dynamics of a decompression [19]; in other words, the outflow velocity equals the speed of sound. This is obtained by solving the Bernoulli equation for the critical pressure under the assumption that $u_{out}(p_c) = c(p_c)$

$$\frac{1}{2}(u_{out}(p_c))^2 + h_{out}(p_c) = \frac{1}{2}u_{in}^2 + h_{in}, \tag{15}$$

where the subscripts *out* and *in* refers to conditions (for the fluid velocity and enthalpy) outside the pipe at the rupture (bore) and just inside the pipe, respectively.

3. Numerical methods and validation

3.1. HEM: Volume of fluid

The Eqs. (1), (2), (3) are solved numerically using MATLAB. First, we write them in vector notation

$$\frac{\partial \mathbf{U}}{\partial t} + \frac{\partial \mathbf{F}(\mathbf{U})}{\partial x} = \mathbf{S}, \tag{16}$$

with,

$$\mathbf{U} = \begin{bmatrix} \rho \\ \rho u \\ E \end{bmatrix}, \quad \mathbf{F}(\mathbf{U}) = \begin{bmatrix} \rho u \\ \rho u^2 + p \\ (E+p)u \end{bmatrix}, \quad \mathbf{S} = \begin{bmatrix} 0 \\ G + f \\ Q + Gu \end{bmatrix}, \tag{17}$$

where $\mathbf{U}$, $\mathbf{F}(\mathbf{U})$, and $\mathbf{S}$ are the conserved variables, the flux, and the source vectors. Then, we discretize the governing equations on a uniform one-dimensional grid of m points with a finite-volume approach, integrating over the cell control volume $[x_{i-\frac{1}{2}}, x_{i+\frac{1}{2}}]$:

$$\frac{d}{dt}\int_{x_{i-\frac{1}{2}}}^{x_{i+\frac{1}{2}}} \mathbf{U}(x,t)\,\mathrm{d}x + \left[\mathbf{F}(\mathbf{U}(x,t))\right]_{x_{i-\frac{1}{2}}}^{x_{i+\frac{1}{2}}} = \int_{x_{i-\frac{1}{2}}}^{x_{i+\frac{1}{2}}} \mathbf{S}(\mathbf{U}(x,t))\,\mathrm{d}x\,, \tag{18}$$

where the variables are assumed constant within the cell and the cell-average as

$$\mathbf{U}_i(t) = \frac{1}{\Delta x}\int_{x_{i-\frac{1}{2}}}^{x_{i+\frac{1}{2}}} \mathbf{U}(x,t)\,\mathrm{d}x, \tag{19}$$

with Δx being the spatial step. The numerical fluxes at the interfaces are evaluated as $\mathbf{F}_{i\pm\frac{1}{2}} \approx \mathbf{F}(\mathbf{U}(x_{i\pm\frac{1}{2}}, t))$ obtaining the semi-discrete form of the HEM

$$\frac{d\,\mathbf{U}_i}{dt} = -\frac{1}{\Delta x}\left(\mathbf{F}_{i+\frac{1}{2}} - \mathbf{F}_{i-\frac{1}{2}}\right) + \mathbf{S}_i. \tag{20}$$

Then, applying the explicit Euler method for time integration, the fully discrete form of the equations in vector notation yields

$$\mathbf{U}_i^{n+1} = \mathbf{U}_i^n - \frac{\Delta t}{\Delta x}\left[\mathbf{F}(\mathbf{U}^n_{i+\frac{1}{2}}) - \mathbf{F}(\mathbf{U}^n_{i-\frac{1}{2}})\right] + \Delta t\,\mathbf{S}_i^n\,, \tag{21}$$

where $\mathbf{U}_i^n$ is the vector of the conserved variables in the ith cell at time step n, and Δt is the time step. We compute the numerical fluxes using the FORCE (First-Order Centered) numerical flux obtained as the average between the Lax–Friedrichs and the Richtmyer fluxes proposed by Toro [47], which is proven to be the least dissipative among first-order centered schemes. Specifically, using the superscripts L and R to indicate the left and right state, or the state of two adjacent cells, the numerical flux according to Lax–Friedrichs [48] is

$$F^{LF}_{i+1/2} = F^{LF}(U_L, U_R) = \frac{1}{2}[F(U_L) + F(U_R)] + \frac{1}{2}\frac{\Delta x}{\Delta t}(U_L - U_R), \tag{22}$$

while the Richtmyer scheme [49] derives the numerical flux by defining an intermediate state

$$U^R_{i+1/2} = U^R(U_L, U_R) = \frac{1}{2}(U_L + U_R) + \frac{1}{2}\frac{\Delta t}{\Delta x}(F(U_L) - F(U_R))\,, \tag{23}$$

and, then, setting

$$F^R_{i+1/2} = F(U^R_{i+1/2}). \tag{24}$$

Thus the first-order centered (FORCE) scheme is given by

$$F^{FORCE}_{i+1/2} = F^{FORCE}(U_L, U_R) = \frac{1}{2}[F^{LF}(U_L, U_R) + F^R(U_L, U_R)]. \tag{25}$$

The time step is computed in an adaptive way based on the local speed of sound and setting the Courant number to $CFL = 0.85$ as

$$\Delta t = \min(\Delta t_i) \qquad \Delta t_i = \frac{CFL\,\Delta x}{|u_i + c_i|}\,. \tag{26}$$

The heat equation, Eq. (11), accounting for the heat transfer between the fluid and the surroundings is solved numerically as described in Appendix A and, then, coupled with the volume of fluids code for HEM.

3.2. Experimental validation

Our numerical code has been validated with the experimental data obtained in the ECCSEL depressurization facility by Munkejord et al. [11]. These depressurization experiments consist of a pipeline filled with CO_2 and equipped with temperature and pressure transducers at multiple pipe locations and designed to span various initial conditions in terms of temperature and pressure. At one end of the pipe, in fact, is situated a rupture disk designed to break at a specific pressure, leading to the depressurization of the line. Specifically, we replicate the experiments listed in Table 1 and analyze the flow evolution at 0.001, 0.01, 0.1, and 1.0 s after the onset of depressurization. The numerical grid used for these tests consists of 1500 points, and a CFL number of 0.85 is enforced (the grid convergence test is presented in Appendix B). As can be seen from Fig. 2, the results show a good agreement with the experimental data, confirming that the HEM satisfactorily captures the pressure evolution of depressurization, including the transition to two-phase flows as shown also by Munkejord et al. [11] and Log et al. [42].

Table 1
Initial conditions used for the validation with the experiments by Munkejord et al. [11].

Test no.	Fluid	p_0 (MPa)	T_0 (°C)	T_{amb} (°C)	Initial state
4	CO_2	12.54	21.1	22	Liquid
6	CO_2	10.4	40.0	6	Supercritical
8	CO_2	12.22	24.6	9	Liquid

4. Model for the running ductile fracture

In this section we summarize the fracture model to predict the pipeline failure during the depressurization. The key mechanism is the running ductile fracture (RDF), namely a failure where a crack (originally initiated by corrosion or accidental events) initiates and propagates rapidly along the pipe wall [50]. The propagation is sustained by the decompression wave that travels with the crack, and it arrests only when the pressure (driving) force balances with the pipe resistance to fracture.

Specifically, we adopt the Battelle Two-Curve Method (BTCM) [12], a well-known model originally developed for natural gas to estimate whether a ductile fracture will propagate or arrest. The idea is to compare the decompression wave speed of the fluid inside the pipeline with the crack-tip velocity of the pipe wall. This critical speed is estimated from the curve of the material that relates the crack-tip pressure p_{ct} to the crack-tip velocity u_{ct} as

$$p_{ct} = p_a\left[1 + \left(\frac{u_{ct}\sqrt{\frac{\mathrm{CVN}}{A}}}{K_{\mathrm{BF}}\,\sigma}\right)^6\right], \tag{27}$$

where p_a is the arrest pressure [Pa], u_{ct} is the crack-tip velocity [m/s], CVN is the Charpy V-notch energy [J], A is the Charpy specimen cross-section area [m^2], K_{BF} is the backfill parameter (assumed $9E-4$ considering a non-buried pipe case scenario) [$kg^2\ m^{0.5}$], σ is the flow stress defined as $\sigma = \sigma_{ys} + 68.95$ MPa. The arrest pressure is modeled following the Strip-Yield model

$$p_a = \frac{2\sigma s}{M_T \pi r_o}\arccos\left[\exp\left(-\frac{K^2_{mat}\pi}{8a_c\sigma^2}\right)\right], \tag{28}$$

where s is the wall thickness [m], r_o is the pipe outer radius [m], $a_c = 3\sqrt{r_o s}$ is the effective value accounting for the half-length of the through-wall propagating crack [m] M_T is the Folias factor, K_{mat} is the material toughness parameter [J/m^2] computed using the Toughness–CVN relation $K_{mat} = \sqrt{\mathcal{E}\frac{\mathrm{CVN}}{A}}$, $\mathcal{E}$ is the Young's modulus of the pipe material, and the Folias Factor is given by

$$M_T = \sqrt{1 + 1.255\frac{a_c^2}{r_o s} - 0.0135\frac{a_c^4}{r_o^2 s^2}}\,. \tag{29}$$

The decompression wave speed w is defined as the difference between the sound speed, Eq. (8), and the fluid speed in the pipeline, u, obtained from the depressurization simulation as in [14]

$$w(p) = c(p) - u(p)\,, \tag{30}$$

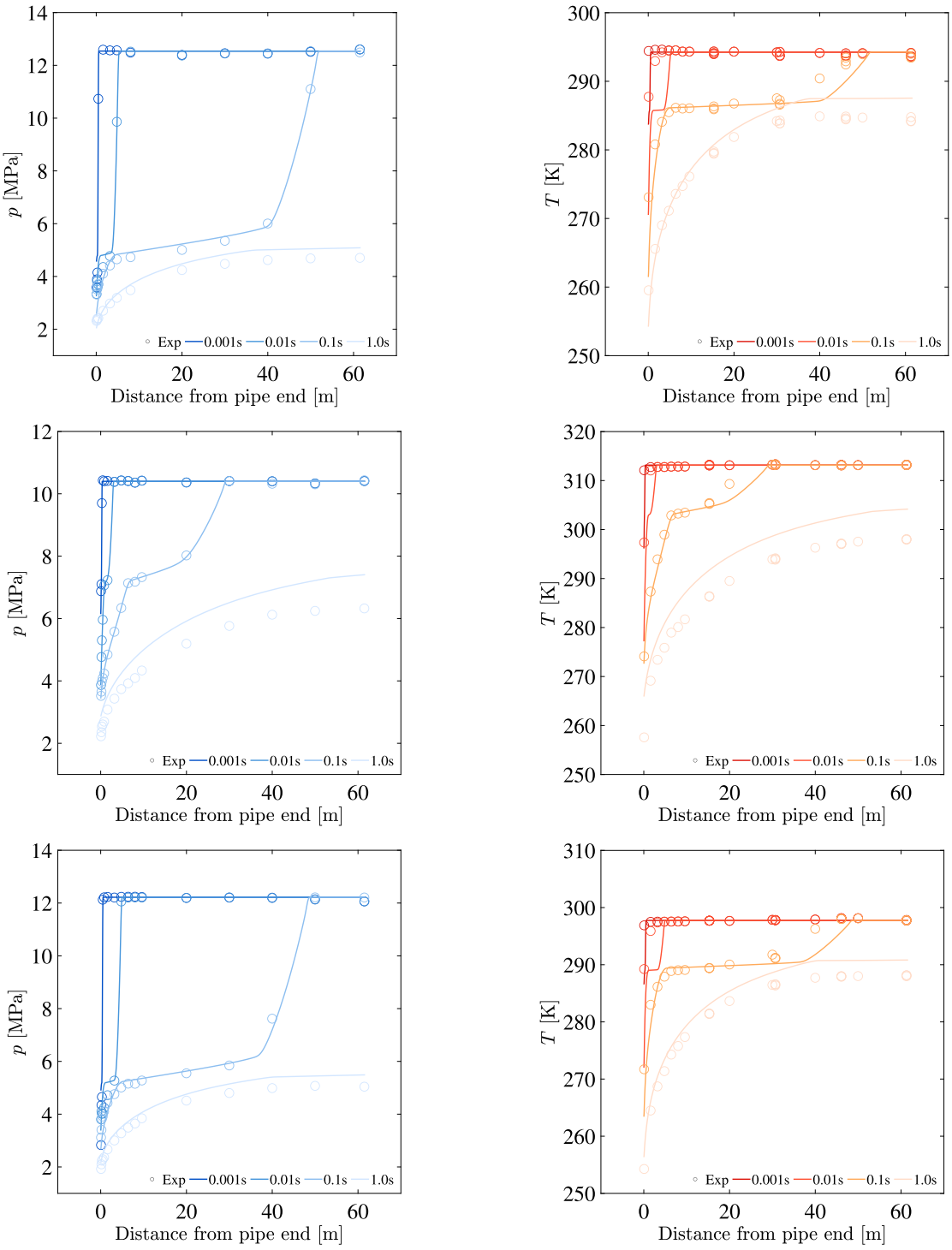

Fig. 2. Model validation with the experiments in [11] listed in Table 1. The solid points are the experiments data while the continuous lines are the pressure and temperature fields obtained from the simulations, plotted at different times. Experiment 4 (row 1), 6 (row 2) and 8 (row 3).

that we estimate using the HEM simulations as described in Section 2. In Fig. 3 we show the comparison between the experiments of Munkejord et al. [11] and our simulations, showing that the HEM satisfactorily predicts the evolution of the decompression wave speed. Only for the purpose of comparison, since usually BTCM analyses are performed with a simplified isentropic decompression model, we also present the isentropic decompression curve obtained using RAMDECOM [51].

Once the material curve and the decompression wave speed are plotted in the $w - p$ plane, the Battelle Two-Curve Method works as follows. In case the material curve (in terms of p_{cl} and w) and the CO_2 curve (in terms of p and w) do not meet as in Fig. 4(a), the model does not predict any pipeline failure. In other words, the moving decompression wave front outruns the propagating crack tip and the driving force supplied by the expanding CO_2 is not sufficient to sustain the fracture propagation. Therefore, the crack is rapidly arrested. Instead, if the two curves intersect as in Fig. 4(b), at the intersection point, the velocity of the decompression wave front and the crack tip propagation velocity become comparable. In this case, the escaping gas pressure acting at the crack tip provides enough energy to overcome the pipe wall resistance and the crack becomes self-sustaining. Specifically,

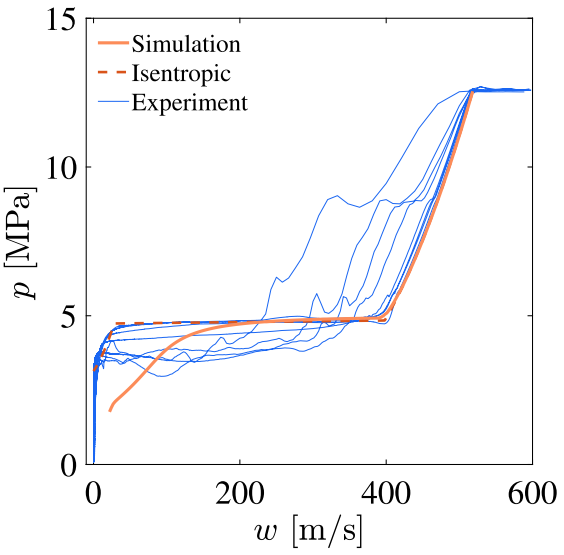

Fig. 3. Plot of the decompression wave speed for pure carbon dioxide obtained from the Experiment 4 by Munkejord et al. [11] listed in Table 1, the HEM simulation with Wood's speed of sound and the isentropic depressurization case for comparison.

the fracture propagates along the pipeline until the gas pressure drops enough to arrest it or other arresting mechanisms intervene.

In the following, in order to systematically identify whether the pipeline is at risk of failure during the depressurization, we introduce a test metric, d_{BTCM}, based on the distance between those curves. Specifically, when the curves does not intersect we take the minimum distance between the curves as shown in Fig. 4(a), while if the two curves meet as in Fig. 4(b), we consider the maximum distance to the right of their point of intersection.

5. Surrogate models

We consider a generic quantity of interest (QoI), y^{HEM}, provided by the numerical high-fidelity model (namely the equilibrium model HEM in this work) and analyze the effect of the variability in the two governing parameters, p_0 and T_0, i.e., the initial conditions. The ranges of variation covering a significant set of operation conditions for the parameters are described probabilistically using uniform distributions. Alternatively, normal distributions are used for risk assessment purposes around a specific operation condition.

According to the Polynomial Chaos Expansion (PCE) theory (e.g. [29,33]), y^{HEM}, if its variance is finite, can be approximated in the space of the parameters in $\mathbf{p}$ as follows:

$$y^{\mathrm{PCE}} = \sum_{j=0}^{P-1} s_j \boldsymbol{\Psi}_j(\mathbf{p}), \tag{31}$$

where $\boldsymbol{\Psi}_j$ are q-order (in our case $q = 2$) multivariate polynomials — Legendre polynomials in case of uniform distributions, Hermite polynomials in case of normal distributions — $P = (q+M)/q!/M! = 6$, being $M = dim(\mathbf{p}) = 2$.

Coefficients s_j are the deterministic coordinates of the spectral decomposition, computed through a non-intrusive approach based on regression, that minimizes the variance of the residuals between the high-fidelity model predictions and the PCE approximations [32,53]. The regression is carried out on an optimal set of N points selected via the probabilistic collocation method (PCM) [54], which relies on the roots of the polynomial of order $q+1$ to ensure appropriate sampling of the region associated with the largest probability in the distributions of the input parameters (e.g. [29,31]).

Table 2
Summary of the data of the Cortez and Weyburn pipelines used to perform our calculations [52]. The insulation layer is assumed to be a 5 mm (HDPE) High-Density Polyethylene coating, while the employed wall thickness is the minimum within the specified range.

Property	Cortez	Weyburn
Country	USA	CA
Length (nominal) [km]	808	330
Length (simulated) [m]	150	150
Diameter(outer) [mm]	762	356
Steel	X65	X65
Wall thickness [mm]	17.5 to 25.4	9.5 to 15.9
E [GPa]	210	210
Min γ [MPa]	450	450
JCV [J/mm^2]	0.96	0.96
Steel density [kg/m^3]	7850	7850
Steel conductivity [W/m K]	42	42
Steel specific heat capacity [J/kg K]	450	450
Insulation	HDPE	HDPE
Insul. thickness [mm]	5	5
Insul. density [kg/m^3]	956	956
Insul. conductivity [W/m K]	0.4	0.4
Insul. specific heat capacity [J/kg K]	2000	2000

In this study, calibration of the polynomial approximation was performed using only $N = P = 6$ collocation points. Consequently, six high-fidelity simulations were sufficient to construct the PCE surrogate for each QoI, yielding substantial computational efficiency. Once the PCE approximations of the QoIs are available, sensitivity metrics can be obtained through analytical post-processing of the PCE coefficients, as shown in [33,53]. GSA can therefore be carried out on the surrogate model at negligible computational cost, avoiding the need for expensive Monte Carlo simulations of the HEM [29,30]. Specifically, we compute the sensitivity indices of Sobol [55] analytically from the PCE coefficients to quantify the influence of the input parameters, p_0 and T_0, on the model variance of each QoI.

6. Results and discussion

6.1. Scenarios and metrics used for the PCE analysis

We perform a PCE analysis on two scenarios in order to quantify (i) the RDF domain and failure-related metrics under variability in the inlet conditions, and (ii) how uncertainty in these conditions affects the flow characteristics during depressurization. To do so, we define a few metrics based on the HEM outputs. Specifically, we consider the distance, d_{BTCM}, between the material curve and the depressurization in the $p-w$ plane as explained in Section 4, and the minimum temperature, T_{min}, reached during the 1-second of the depressurization, which is linked with the material resistance (e.g., brittle behavior). We also compute the mass of CO_2 discharged into the environment during a 1-second full-bore depressurization, which is relevant for the safety of the infrastructure [7], defined as

$$m_{\mathrm{CO_2}} = \pi r_i^2 \int_0^1 \rho(t)u(t)\, dt\,. \tag{32}$$

Our simulations are based on two existing and well-documented facilities, namely the Cortez and the Weyburn pipelines [3] whose specifications are listed in Table 2. For the two plants considered, we identified a plausible range of initial operating conditions typical of carbon dioxide transport in pressurized pipelines (see e.g., [56]), p_0 and T_0, reported in Table 3.

6.2. Pipeline susceptibility to running ductile fracture

In this Section, we analyze the results of the PCE, considering as QoI the distance between the material and the depressurization

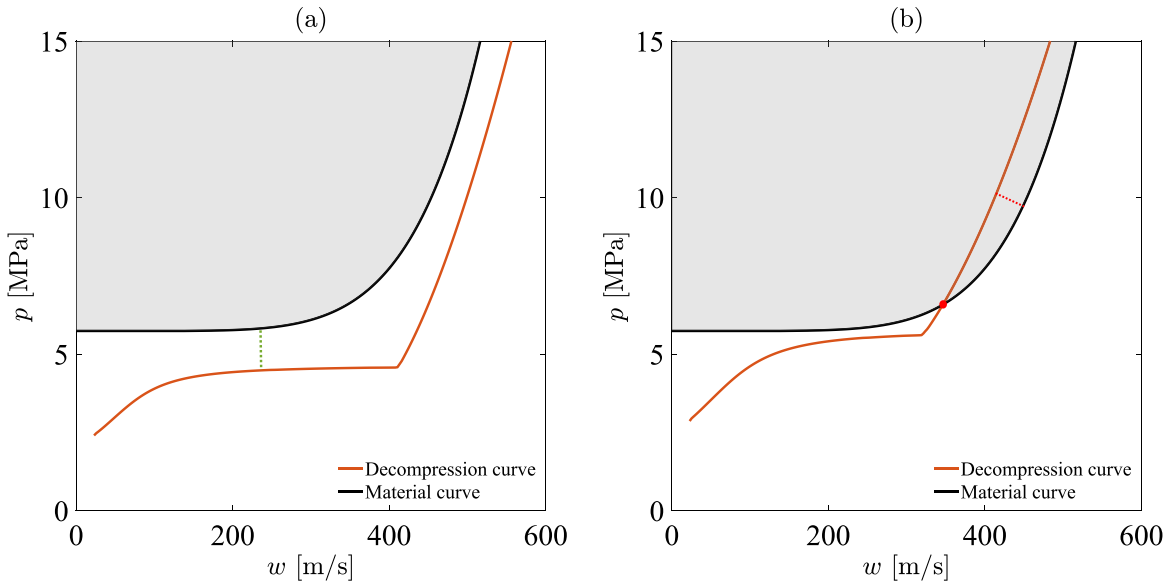

Fig. 4. Examples of distance calculation in the BTCM analysis: no intersection and no pipe rupture (a), and intersection with pipe failure (b). The black curve represents the Cortez pipeline material curve, while the red line shows an example of a simulated CO_2 decompression curve, starting from an initial pressure of $p_0 = 15.6$ MPa and initial temperatures of $T_0 = 21.5°C$ for the case (a) and $T_0 = 32.25°C$ for the case (b).

Table 3
Inlet operating conditions: scenarios of variability.

Property	Fracture	Depressurization
p_0 [MPa]	$\mathcal{U}[9.6, 18.6]$	$\mathcal{N}(11,\ 1.1^2)$
T_0 [°C]	$\mathcal{U}[0, 43]$	$\mathcal{N}(25,\ 2.5^2)$

Table 4
PCE coefficients for each QoI.

QoI	Cortez			Weyburn		
	d_{BTCM}	T_{min}	$m_{\mathrm{CO_2}}$	d_{BTCM}	T_{min}	$m_{\mathrm{CO_2}}$
a_0	−2.157	259.739	11 187.028	20.819	257.861	2358.217
a_1	4.235	0.387	1 234.255	3.450	1.033	256.198
a_2	−50.136	12.975	1 610.516	−44.712	11.813	330.624
a_3	−0.904	0.222	35.611	−0.403	−1.183E−13	4.278
a_4	3.884	−0.833	127.333	2.348	−0.333	33.667
a_5	−27.749	0.056	−82.556	−22.997	−0.278	−19.444

curves, d_{BTCM} (see Section 4), which indicates whether the pipeline is susceptible to running ductile fracture.

To mimic possible variation in the range of design options, the input variables, p_0 and T_0, are modeled as independent random variables uniformly distributed within the ranges reported in Table 3. This type of input variability induces the use of multivariate Legendre polynomials in Eq. (31), leading to the following second-order polynomial approximation of the QoI:

$$d_{\mathrm{BTCM}}^{\mathrm{PCE}} = a_0 + a_1\tilde{p}_0 + a_2\tilde{T}_0 + \frac{a_3}{2}(3\tilde{p}_0^2 - 1) + a_4\tilde{p}_0\tilde{T}_0 + \frac{a_5}{2}(3\tilde{T}_0^2 - 1), \quad (33)$$

where $\tilde{p}_0$ and $\tilde{T}_0$ are the standardized uniform random variables, obtained from p_0 and T_0 through an isoprobabilistic transform [53]. The values of the PCE coefficients, a_j, computed with $P = 6$ high-fidelity simulations serving as the optimal set of regression points, are listed in Table 4.

Thus, Eq. (33) is the surrogate model that enables the reconstruction of the d_{BTCM} map in the (p_0, T_0) space, (see Fig. 5(a) and (c)). To verify the robustness of the surrogate model, we performed the validation of the PCE surrogates against the HEM predictions for 30 combinations of p_0, T_0, sampled in the parameter space as shown in Fig. 5(b) and (d). Since most points lie within or near the 95% confidence bounds, this indicates that the integration of the HEM with the PCE can reach a strong accuracy with only 6 collocation points used to construct the PCE model. Interestingly, the maps in Fig. 5(a) and (c) reveal the RDF domain representing conditions where the pipeline is susceptible to running ductile fracture (defined by $d_{\mathrm{BTCM}} \leq 0$) for both the scenarios summarized in Table 2. We observe that d_{BTCM} is primarily sensitive to variations in the temperature T_0 and, for both plants, the critical conditions occur at high T_0 values within the examined range, but the extent of the RDF domain differs between the two cases. Specifically, the Weyburn plant exhibits a wider safe range of T_0 values where running ductile fracture does not occur, i.e., for temperatures less than about 31°C, compared to the Cortez pipeline, where RDF is prevented only for initial temperatures less than about 26°C. This difference can be primarily attributed to variations in pipeline diameter and wall thickness.

A larger pipeline diameter broadens the range of vulnerability to RDF. This is clearly illustrated in Fig. 6(a), where the material and depressurization curves are shown for both the Cortez and Weyburn pipelines. The simulations refer to a case with $p_0 = 15.6$ MPa, while T_0 ranges from 10.75 to 43.00°C. Since the depressurization is very fast, the $p - w$ depressurization curves are almost identical for the two pipelines except for small differences at low pressures in the two-phase flow region. However, the material curves differ significantly between the two cases as described by Eqs. (27) and (28). The crack-tip pressure p_{ct} is a function of both the pipe thickness s and pipe outer radius r_o, see Fig. 1. Specifically, since the term arcos in Eq. (28) is of $\mathcal{O}(1)$, the crack-tip pressure scales linearly with the thickness, $p_{ct} \sim s$, and decreases with the pipe radius as $p_{ct} \sim r_o^{-1}$. Fig. 6(b) shows that the material curve shifts downward in the $p - w$ plane while increasing both the diameter and the wall thickness (namely from Weburh to Cortez). The inset provides the evolution of the arrest pressure in the BTCM with the outer radius of the pipeline. In general, larger radii increase the stresses in the pipeline section and consequently expand the RDF domain. This trend holds in the whole range of initial pressure considered in Table 3 as confirmed in Fig. 7 for both scenarios for two different values of the initial pressure (p_0 = 12.6 and 15.6 MPa). We can observe that a decrease in p_0 slightly shifts the curves upward, but the overall behavior (namely if the RDf occurs or not) is not really affected by that. Instead, increasing the inlet temperature T_0 shifts the depressurization curves to the left towards the material curve, and, therefore, increases the probability of running ductile fracture as predicted by the surrogate model in Fig. 5.

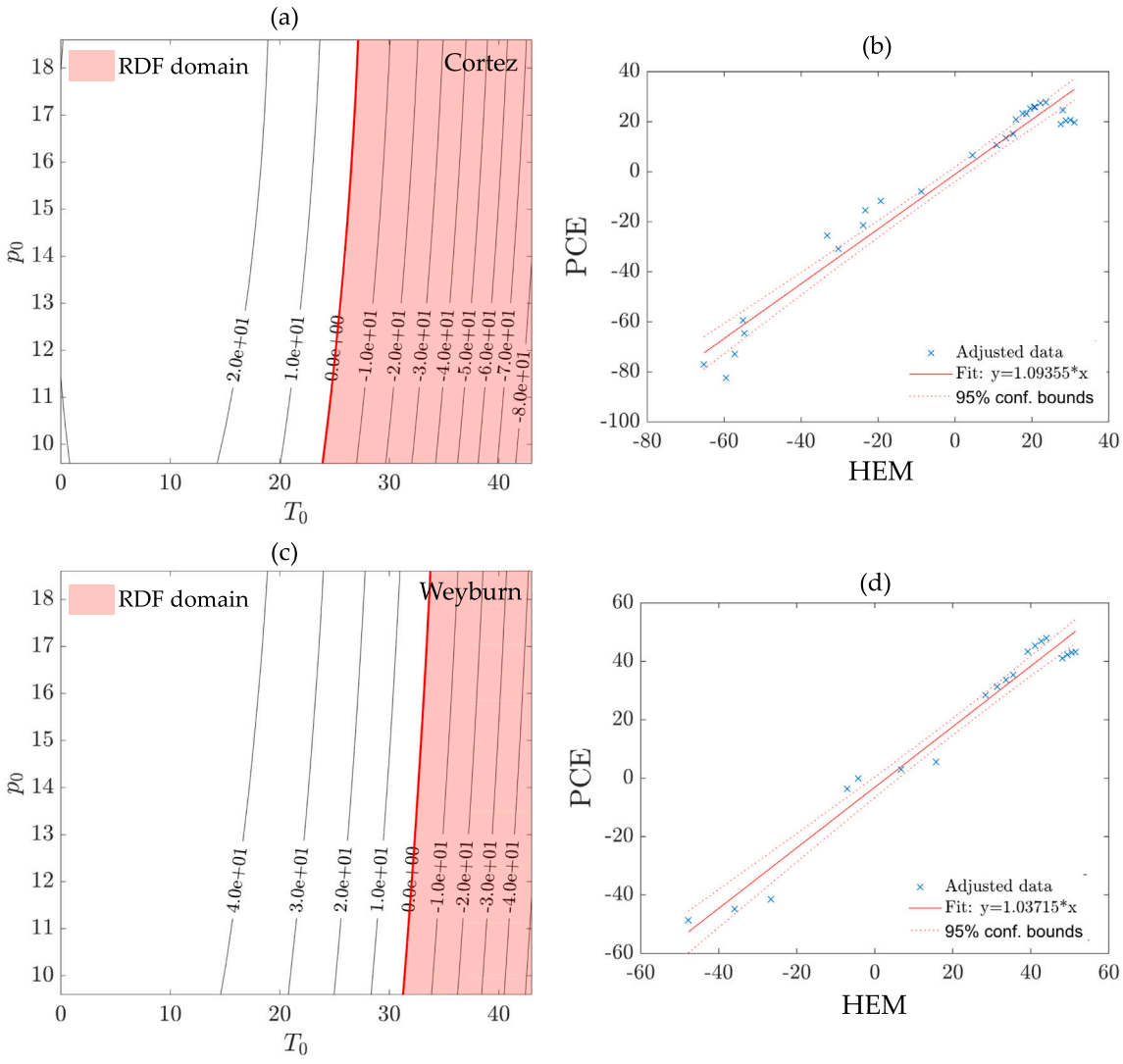

Fig. 5. Running ductile fracture (RDF) domain in the (T_0, p_0) space based on BTCM for the Cortez (a), and Weyburn (c) plants, computed through the PCE surrogates. The validation of the surrogates is performed against the HEM for 30 combinations of (T_0, p_0) sampled in their space of variability in panels (b) and (d).

We also reconstructed the maps for other two QoIs, T_{min} and m_{CO_2}, in the (T_0, p_0) parameter space (see Fig. 8). The PCE surrogates T_{min}^{PCE} and $m_{CO_2}^{PCE}$ follow the same formulation as Eq. (33), with the corresponding coefficients a_j reported in Table 4. In particular, T_{min} is the minimum temperature reached at the opening during depressurization and is related to the brittle transition temperature of the material (steel, in this scenario). In the context of risk assessment for CO_2 transport, in fact, the temperature evolution during a full-bore pipe depressurization deserves particular attention [57] since it may lead to a shift toward a brittle failure mechanism, with significant implications for pipeline operations and integrity [58]. In both the scenarios, T_{min} varies primarily with T_0 with T_{min} increasing as T_0 increases, as expected. To quantify these dependencies, we compute the total sensitivity indices of Sobol through the PCE [29], confirming that the uncertainty in T_{min} is entirely attributable to T_0, see Table 5, while its coefficients of variation is approximately 0.6%.

The discharged mass m_{CO_2} represents the mass of CO_2 discharged by the pipeline during a 1 s full-bore rupture [59], serving as a potentially useful input for other risk assessment models. For example, it can be used to define the safety zone around the pipeline or to calculate the duration of the risk zone in the event of an accident, i.e., the time required for CO_2 levels to fall below a given threshold [60].

Table 5
Results of the uncertainty quantification and the global sensitivity analysis for T_{min} (K) and m_{CO_2} (kg), for the Cortez and Weyburn plants.

Pipeline	QoI	Mean	Variance	ST_{p_0}	ST_{T_0}
Cortez	T_{min}	261.82	2.62	0.0035	1.00
Cortez	m_{CO_2}	10 616.07	121 670	0.79	0.21
Weyburn	T_{min}	259.18	1.99	0.034	0.97
Weyburn	m_{CO_2}	2237.55	5402.56	0.81	0.19

Specifically, m_{CO_2} depends on both T_0 and p_0, increasing with both the initial temperature and pressure. Its uncertainty is approximately 80% driven by p_0 for both plants, see Table 5, and its coefficients of variation is about 3.3% for m_{CO_2}. In addition, note that, for the Cortez plant, m_{CO_2} is approximately one order of magnitude higher, consistent with the fact that its diameter is almost two times that of the Weyburn one.

6.3. Variability of flow during depressurization

In this section, we examine the evolution of the main flow variables during the depressurization. Specifically, we analyze the pressure,

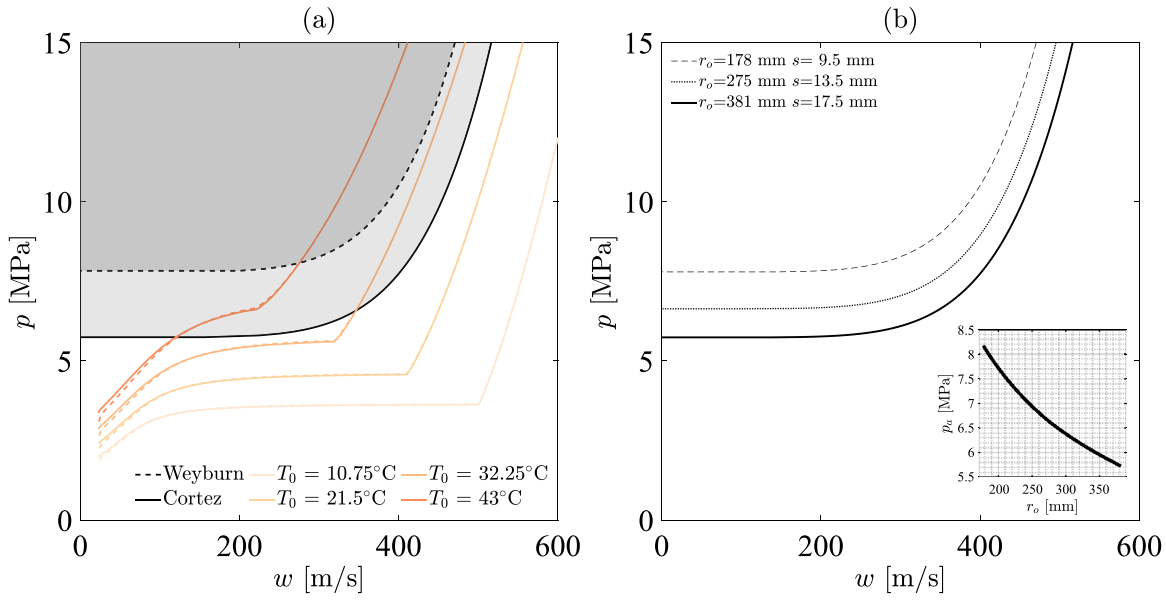

Fig. 6. (a) BTCM curves in the $p-w$ plane for two scenarios: solid line (Cortez) and dashed lines (Weyburn). The plots show both the material curve and the conditions where the RDF is possible and the depressurization curves obtained with the HEM initialized at $p_0 = 15.6$ MPa and different temperatures. (b) Effect of the pipe outer radius r_o and its thickness s on the material curve; the inset shows the effect of r_o on the arrest pressure p_a in the BTCM model.

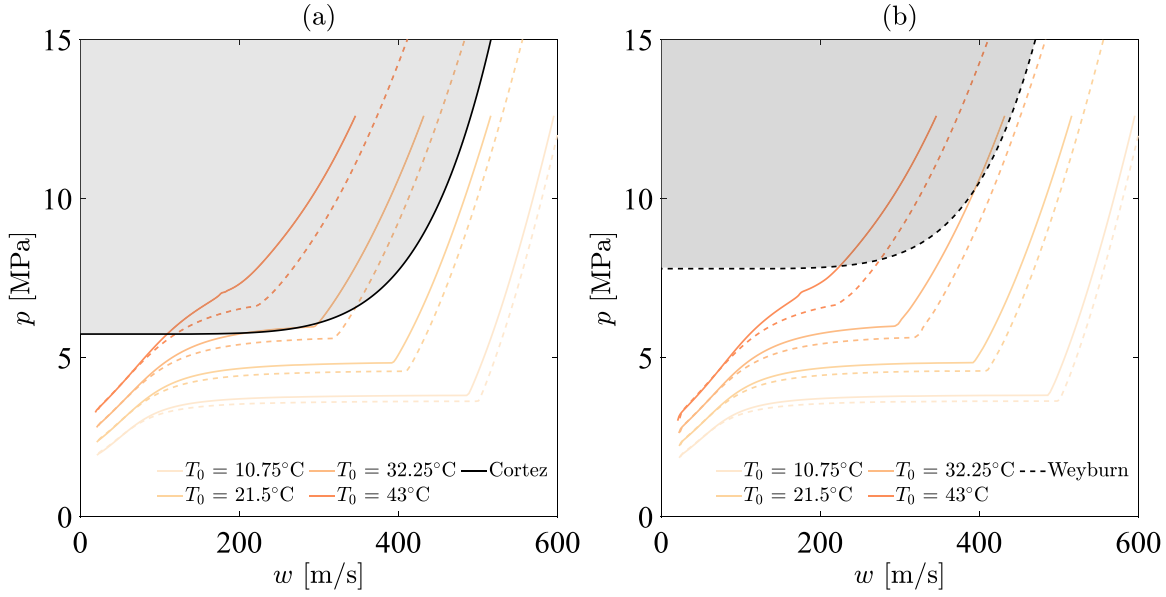

Fig. 7. BTCM curves comparison at 12.6 MPa (solid line) and 15.6 MPa (dashed line) at different temperatures for (a) Cortez pipeline, (b) Weyburn pipeline.

$p(x,t)$, and the temperature, $T(x,t)$, and perform a global sensitivity analysis to assess how the initial conditions, p_0 and T_0, influence the depressurization. To do so, we assume variability around the nominal operating conditions $p_0 = 11$ MPa and $T_0 = 25$°C, modeling the inlet parameters as normally distributed with a coefficient of variation of 10% (see Table 3).

In accordance with the input variability, we selected multivariate Hermite polynomials and derived from Eq. (31) the following second-order polynomial approximation for $p(x,t)$:

$$p(x,t)^{\mathrm{PCE}} = b_0 + b_1\,\tilde{p}_0 + b_2\,\tilde{T}_0 + b_3\,(\tilde{p}_0^2 - 1) + b_4\,\tilde{p}_0\tilde{T}_0 + b_5\,(\tilde{T}_0^2 - 1), \quad (34)$$

where $\tilde{p}_0$ and $\tilde{T}_0$ are the standardized normal random variables obtained through an isoprobabilistic transform from p_0 and T_0, and the PCE coefficients $b_j = b_j(x,t)$ vary in space and time. The same formulation as Eq. (34) holds for the PCE surrogate model of $T(x,t)$, with different values of the coefficients $b_j = b_j(x,t)$. In Fig. 9, the total Sobol sensitivity indices are shown as a function of x for four representative time instants capturing the evolution of the depressurization along the pipeline. First, at early times, the pressure p_0 dominates (over the contribution of T_0) on the variability in both plants. Then, as the depressurization front propagates along the pipeline, the influence of p_0 decreases to about 20%, while the contribution of T_0 increases to about 80%. A similar trend is observed also for the temperature $T(x,t)$ where, at later times, the contribution of p_0 progressively stabilizes around 20%. The only difference is that in this case T_0 is the dominant parameter from the beginning pf the depressurization.

This is supported by the spatial evolution of the temperature and the pressure obtained with the HEM at $t = 0.01$ s and $t = 0.1$ s for different T_0 and p_0 as shown in Fig. 10. We observe that p does not vary with T_0 along the portion of the pipeline that is not yet affected by the

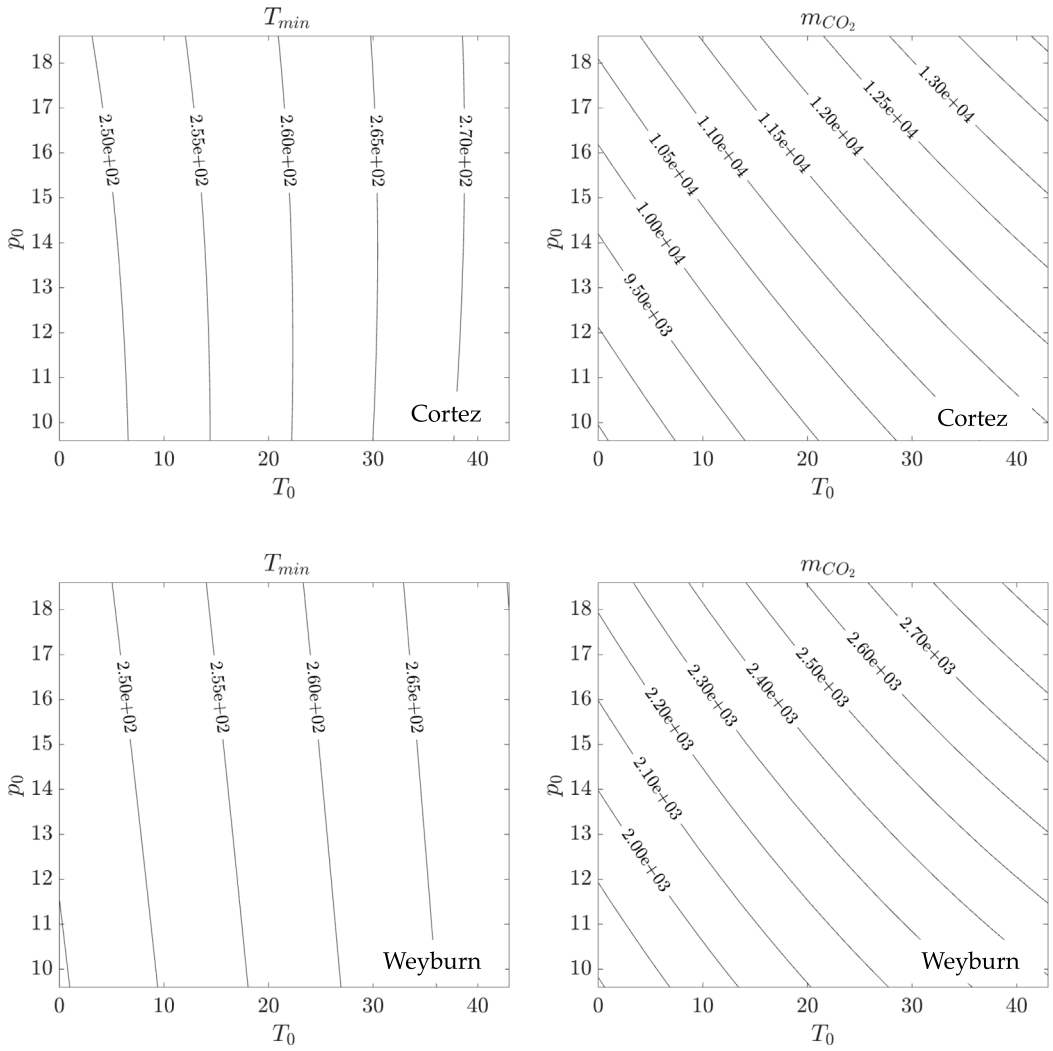

Fig. 8. T_{min} [K] and m_{CO_2} [kg] in the (T_0, p_0) space for the Cortez (first row), and Weyburn (second row) plants, computed through the PCE surrogates.

depressurization front (where its value remains equal to p_0) as in panels (a) and (c). Conversely, where the depressurization front is already passed, the variability of the pressure with respect to different initial temperatures T_0 becomes more evident, see Fig. 10(a). This behavior is even more pronounced, at $t = 0.1$ s.

Similarly, the temperature remains equal to T_0 in regions not yet reached by the depressurization front, while, in the other portion of the pipeline, its variability is mainly due to the effect of the initial temperature T_0. This can be seen in Fig. 10(b) both at early times and late times and demonstrates that the global sensitivity analysis effectively captures the influence of the inlet operating conditions at any time and location during the process, thereby supporting design and operational decisions in the context of transport of carbon dioxide in pipelines.

7. Conclusions

In this work, we developed a framework to analyze the susceptibility of CO_2 pipelines to running ductile fracture (RDF) and to quantify uncertainty in depressurization dynamics using Polynomial Chaos Expansion (PCE) surrogates coupled with a high-fidelity multiphase flow solver based on the Homogeneous Equilibrium Model. Two reference infrastructures — the Cortez and Weyburn pipelines — were used as case studies to investigate both fracture-related metrics and transient flow characteristics.

The analysis shows that pipeline geometry exerts a primary influence on pipeline susceptibility to running ductile fractures. In particular, we show that a larger diameter (and pipe thickness) broadens the range of vulnerability to such type of fracture in the window of operating conditions typical of transport of carbon dioxide (i.e., $T_0 \in [0, 43]$°C and $p_0 \in [9.6, 18.6]$ MPa). This trend is explained by the fact that the material curve in the Battelle Two-Curves Method, which quantifies the critical crack-tip pressure, shifts with increasing pipe diameter so that the pipelines become more susceptible to fracture. In addition, for a given pipe geometry, we show that the driver of fracture risk is the initial temperature (just before the depressurization occurs) rather than the pressure. In other words, only if the temperature is maintained below a certain value ($\approx$ 26°C for the Cortez and $\approx$ 31°C for the Wayburn), the onset of the running ductile fracture is prevented. This is complemented by the analysis of the minimum temperature reached during the depressurization, which becomes important in assessing brittle-to-ductile transitions in pipeline steels. Similarly to the case of the running ductile fractures, the minimal temperature is entirely controlled by the variability of the initial temperature T_0 rather than the initial pressure. Interestingly, the discharged mass, which becomes important in quantifying the risk associated with a CO_2 leak into the environment and in defining the safe zone around the pipeline, depends on both the initial parameters and its magnitude scales with the pipeline diameter, namely larger diameter pipelines represent an increased risk compared to smaller ones.

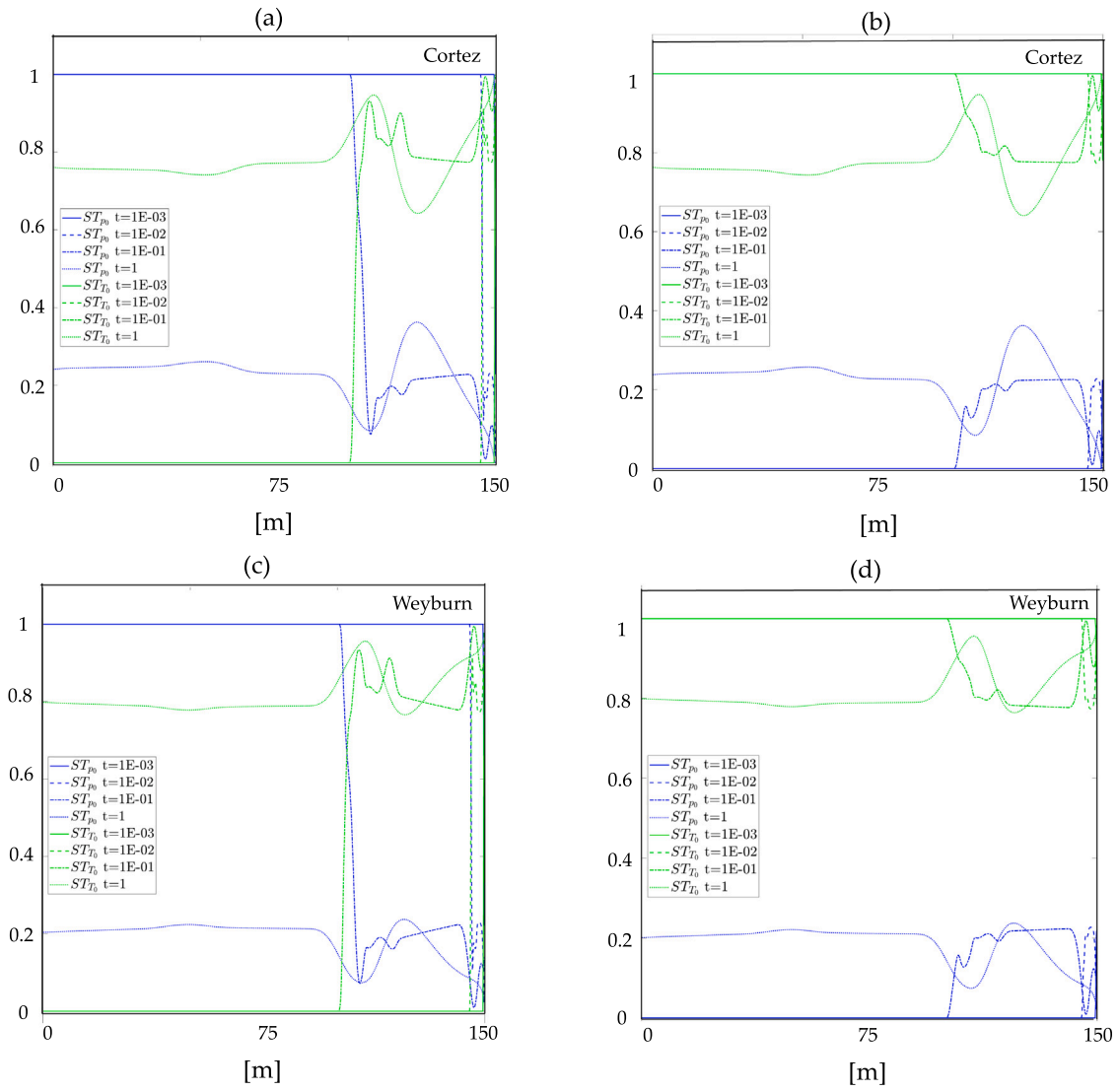

Fig. 9. Total sensitivity indices of Sobol (ST) of p_0, T_0 for the QoIs $p(x)$, panels (a) and (c), and $T(x)$, panels (b) and (d) at t = 1E−03 s, 1E−02 s, 1E−01 s, 1 s, for the Cortez, and Weyburn plants.

The sensitivity analysis of depressurization dynamics further reveals that at the onset of the rupture, the variability in the pressure is dominated by the initial pressure, while, as the depressurization front propagates, the initial temperature becomes the controlling factor. Instead the temperature evolution is primarily governed by the initial temperature rather than the initial pressure.

Overall, these results highlight the capability of PCE surrogates to capture both fracture-related risks and flow dynamics under uncertainty at a fraction of the computational cost of high-fidelity simulations such as the widely used Homogeneous Equilibrium Model. We believe that the proposed approach provides a practical and efficient tool for risk assessment, informing safer design and operation of CO_2 pipeline infrastructures.

CRediT authorship contribution statement

Gabriele Bicelli: Writing – review & editing, Writing – original draft, Validation, Software, Formal analysis, Data curation. **Giulia Libero:** Writing – review & editing, Writing – original draft, Validation, Methodology, Formal analysis, Data curation. **Davide Picchi:** Writing – review & editing, Methodology, Investigation, Funding acquisition, Formal analysis, Conceptualization. **Valentina Ciriello:** Writing – review & editing, Methodology, Funding acquisition, Formal analysis, Conceptualization, Supervision.

Declaration of competing interest

The authors declare that they have no known competing financial interests or personal relationships that could have appeared to influence the work reported in this paper.

Acknowledgments

This study has received funding from the European Union “NextGenerationEU”, Ministero dell’Università e della Ricerca (MUR) “Italiadomani” Piano Nazionale di Ripresa e Resilienza (PNRR), Mission 4, Research Project PRIN 2022 “Predictive forecasting and risk assessment for CO2 transport in pipelines”, MUR code: 20229JPN53; CUP code: J53D2300200 0006; CUP code: D53D23003250006.

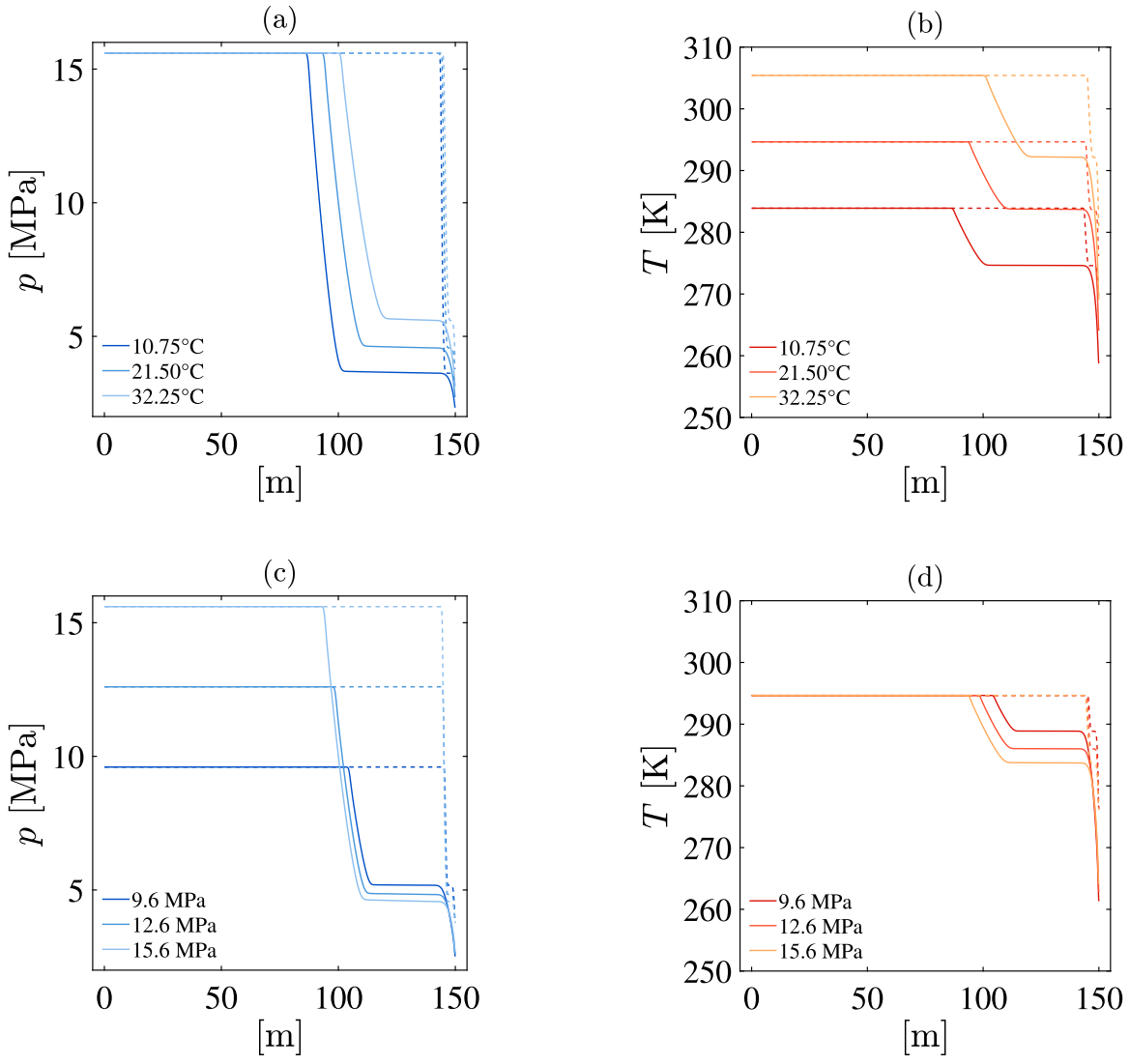

Fig. 10. Evolution of pressure and temperature at $t = 0.01$ s (dashed line) and $t = 0.1$ s (solid line) for different initial values of T_0 and p_0 in the Cortez pipeline. (a) and (b) $p_0 = 15.6$ MPa while T_0 varies; (c) and (d) $T_0 = 21.5$°C while p_0 varies.

Appendix A. Discretization of the heat equation

In order to obtain the wall temperature and compute the heat transfer source term Q in Eq. (3), the heat equation in the radial direction within the pipe and its insulation layer, Eq. (11), is solved using the central finite difference method as

$$\hat{T}_i^{n+1} = \hat{T}_i^n + \frac{\hat{\kappa}_i}{\hat{\rho}\hat{c}_p}\,\Delta t\left[\frac{1}{r_i}\,\frac{\hat{T}_{i+1}^n - \hat{T}_{i-1}^n}{2\,\Delta r} + \frac{\hat{T}_{i+1}^n - 2\,\hat{T}_i^n + \hat{T}_{i-1}^n}{\Delta r^2}\right]. \tag{A.1}$$

where $\hat{T}_i^n \approx \hat{T}(r_i, t^n)$ is the temperature at radial node i and time-level n and

$$\Delta r = \frac{r_{\text{ins}} - r_{\text{i}}}{N}, \quad t^n = n\,\Delta t, \tag{A.2}$$

and the thermal properties are defined only in the interior nodes ($i = 2, \ldots, N-1$). Being T_0, T_{N+1} be the ghost-point temperatures, we enforce the convective boundary conditions

$$\hat{T}_0^n = \hat{T}_1^n + \frac{\Delta r\, h_{\text{i}}}{\hat{\kappa}_{\text{pipe}}}\left(\hat{T}_1^n - T_{\text{i}}\right), \qquad \text{at} \quad r = r_{\text{in}} \tag{A.3}$$

$$\hat{T}_{N+1}^n = \hat{T}_N^n - \frac{\Delta r\, h_{\text{ins}}}{\hat{\kappa}_{\text{ins}}}\left(\hat{T}_N^n - T_{amb}\right) \qquad \text{at} \quad r = r_{\text{ins}}\,. \tag{A.4}$$

Appendix B. Grid convergence

For the sake of validation, we also show the grid convergence study, performed on Experiment 4 listed in Table 1 at 0.1 s after the onset of depressurization. In Fig. B.11, the model predictions are plotted for increasing levels of grid refinement (namely, 500, 1000, 2500, 5000, and 10 000 grid points), showing that already a grid of 1500 is sufficient to lower the pressure relative error below 1% compared to the 10 000 grid points case.

Data availability

Data will be made available on request.

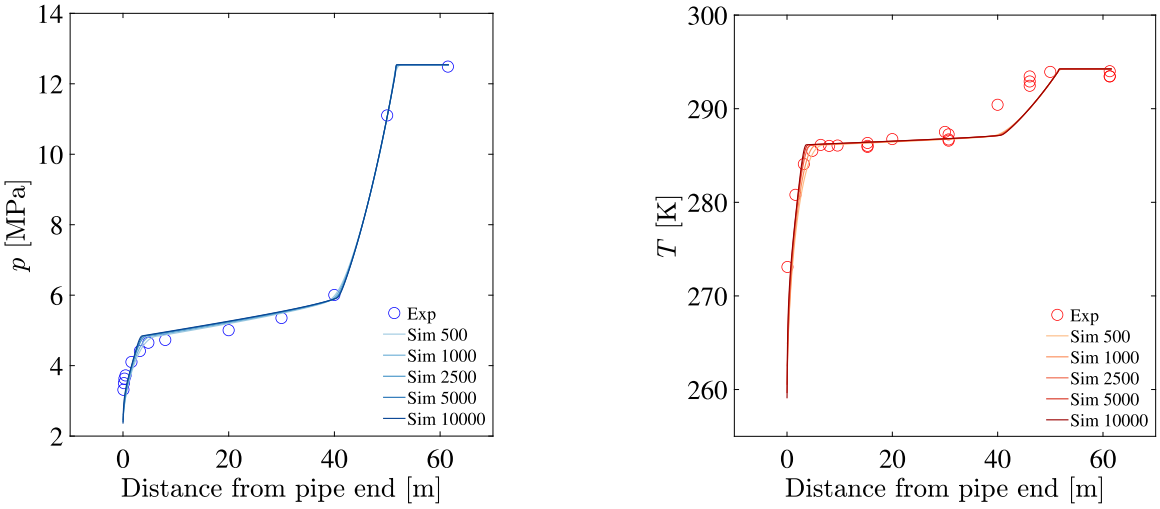

Fig. B.11. Grid convergence test on pressure and temperature evolutions performed on Experiment 4 listed in Table 1 from the work of Munkejord et al. [11].

References

[1] IEA. Net zero roadmap: A global pathway to keep the 1.5 ° C goal in reach - 2023 Update. IEA Rep 2023.

[2] Munkejord ST, Hammer M, Løvseth SW. CO2 transport: Data and models – A review. Appl Energy 2016;169:499–523. http://dx.doi.org/10.1016/j.apenergy.2016.01.100.

[3] Peletiri S, Rahmanian N, Mujtaba I. CO2 pipeline design: A review. Energies 2018;11(9):2184. http://dx.doi.org/10.3390/en11092184.

[4] Onyebuchi V, Kolios A, Hanak D, Biliyok C, Manovic V. A systematic review of key challenges of CO2 transport via pipelines. Renew Sustain Energy Rev 2018;81:2563–83. http://dx.doi.org/10.1016/j.rser.2017.06.064.

[5] Vitali M, Corvaro F, Marchetti B, Terenzi A. Thermodynamic challenges for CO2 pipelines design: A critical review on the effects of impurities, water content, and low temperature. Int J Greenh Gas Control 2022;114:103605. http://dx.doi.org/10.1016/j.ijggc.2022.103605.

[6] Noothout P, Wiersma F, Hurtado O, Macdonald D, Kemper J, Van Alphen K. CO2 pipeline infrastructure – Lessons learnt. Energy Procedia 2014;63:2481–92. http://dx.doi.org/10.1016/j.egypro.2014.11.271.

[7] Koornneef J, Spruijt M, Molag M, Ramírez A, Turkenburg W, Faaij A. Quantitative risk assessment of CO2 transport by pipelines—A review of uncertainties and their impacts. J Hazard Mater 2010;177(1–3):12–27. http://dx.doi.org/10.1016/j.jhazmat.2009.11.068.

[8] Zhang Z, Wang G, Massarotto P, Rudolph V. Optimization of pipeline transport for CO2 sequestration. Energy Convers Manage 2006;47(6):702–15. http://dx.doi.org/10.1016/j.enconman.2005.06.001.

[9] Lund H, Flåtten T, Tollak Munkejord S. Depressurization of carbon dioxide in pipelines–Models and methods. Energy Procedia 2011;4:2984–91. http://dx.doi.org/10.1016/j.egypro.2011.02.208.

[10] Dixon CM, Gant SE, Obiorah C, Bilio M. Validation of dispersion models for high pressure carbon dioxide releases. 2012.

[11] Munkejord ST, Austegard A, Deng H, Hammer M, Stang HJ, Løvseth SW. Depressurization of CO2 in a pipe: High-resolution pressure and temperature data and comparison with model predictions. Energy 2020;211:118560. http://dx.doi.org/10.1016/j.energy.2020.118560.

[12] Maxey W, Kiefner J, Eiber R, Duffy A. Ductile fracture initiation, propagation, and arrest in cylindrical vessels. In: Fracture toughness: part II. ASTM International100 Barr Harbor Drive, PO Box C700, West Conshohocken, PA 19428-2959; 1972, p. 70–81. http://dx.doi.org/10.1520/STP38819S.

[13] Hu Q, Zhang N, Li Y, Wang W, Zhu J, Gong J. A new model for calculation of arrest toughness in the fracture process of the supercritical CO_2 pipeline. ACS Omega 2021;6(26):16804–15. http://dx.doi.org/10.1021/acsomega.1c01360, Publisher: American Chemical Society (ACS).

[14] Skarsvåg HL, Hammer M, Munkejord ST, Log AM, Dumoulin S, Gruben G. Towards an engineering tool for the prediction of running ductile fractures in CO2 pipelines. Process Saf Environ Prot 2023;171:667–79. http://dx.doi.org/10.1016/j.psep.2023.01.054.

[15] De Koeijer G, Borch JH, Jakobsenb J, Drescher M. Experiments and modeling of two-phase transient flow during CO2 pipeline depressurization. Energy Procedia 2009;1(1):1683–9. http://dx.doi.org/10.1016/j.egypro.2009.01.220.

[16] Cosham A, Jones D, Armstrong K, Allason D, Barnett J. The decompression behaviour of carbon dioxide in the dense phase. 2012, http://dx.doi.org/10.1115/IPC2012-90461.

[17] Nordhagen H, Munkejord S, Hammer M, Gruben G, Fourmeau M, Dumoulin S. A fracture-propagation-control model for pipelines transporting CO2-rich mixtures including a new method for material-model calibration. Eng Struct 2017;143:245–60. http://dx.doi.org/10.1016/j.engstruct.2017.04.015.

[18] Yu S, Yan X, He Y, Chen L, Hu Y, Yang K, Cao Z, Yu J, Chen S. Study on the decompression behavior during large-scale pipeline puncture releases of CO_2 with various N_2 compositions: Experiments and mechanism analysis. Energy 2024;296:131180. http://dx.doi.org/10.1016/j.energy.2024.131180.

[19] Munkejord ST, Hammer M. Depressurization of CO2-rich mixtures in pipes: Two-phase flow modelling and comparison with experiments. Int J Greenh Gas Control 2015;37:398–411. http://dx.doi.org/10.1016/j.ijggc.2015.03.029.

[20] Fang Y, De Lorenzo M, Lafon P, Poncet S, Bartosiewicz Y. An accurate and efficient look-up table equation of state for two-phase compressible flow simulations of carbon dioxide. Ind Eng Chem Res 2018;57(22):7676–91. http://dx.doi.org/10.1021/acs.iecr.8b00507.

[21] Kumar P, Sanderse B, Esquivel R, Henkes R. Numerical modelling of two-phase CO2 flow in pipes. In: Proceedings of the 12th North American conference on multiphase production technology. MPNA 2024, 2024.

[22] Picchi D, Ciriello V. Impact of variability in inlet operating conditions on CO2 transport in pipelines. Int J Multiph Flow 2026;196:105556. http://dx.doi.org/10.1016/j.ijmultiphaseflow.2025.105556.

[23] Munkejord ST, Evje S, Flåtten T. The multi-stage centred-scheme approach applied to a drift-flux two-phase flow model. Numer Methods Fluids 2006;52(6):679–705. http://dx.doi.org/10.1002/fld.1200.

[24] Aursand P, Hammer M, Munkejord S, Wilhelmsen Ø. Pipeline transport of CO2 mixtures: Models for transient simulation. Int J Greenh Gas Control 2013;15:174–85. http://dx.doi.org/10.1016/j.ijggc.2013.02.012.

[25] Bruce Stewart H, Wendroff B. Two-phase flow: Models and methods. J Comput Phys 1984;56(3):363–409. http://dx.doi.org/10.1016/0021-9991(84)90103-7.

[26] Brown S, Martynov S, Mahgerefteh H, Chen S, Zhang Y. Modelling the non-equilibrium two-phase flow during depressurisation of CO 2 pipelines. Int J Greenh Gas Control 2014;30:9–18. http://dx.doi.org/10.1016/j.ijggc.2014.08.013.

[27] Lu M, Connell LD. The transient behaviour of CO2 flow with phase transition in injection wells during geological storage – Application to a case study. J Petroleum Sci Eng 2014;124:7–18. http://dx.doi.org/10.1016/j.petrol.2014.09.024.

[28] Hammer M, Morin A. A method for simulating two-phase pipe flow with real equations of state. Comput & Fluids 2014;100:45–58. http://dx.doi.org/10.1016/j.compfluid.2014.04.030.

[29] Ciriello V, Lauriola I, Bonvicini S, Cozzani V, Di Federico V, Tartakovsky DM. Impact of hydrogeological uncertainty on estimation of environmental risks posed by hydrocarbon transportation networks. Water Resour Res 2017;53(11):8686–97. http://dx.doi.org/10.1002/2017wr021368.

[30] Focaccia S, Panini G, Pedrazzoli P, Ciriello V. A meta-modeling approach for hydrological forecasting under uncertainty: Application to groundwater nitrate response to climate change. J Hydrol 2021;603:127173. http://dx.doi.org/10.1016/j.jhydrol.2021.127173.

[31] Libero G, Tartakovsky D, Ciriello V. Polynomial chaos enhanced by dynamic mode decomposition for order-reduction of dynamic models. Adv Water Resour 2024;186:104677. http://dx.doi.org/10.1016/j.advwatres.2024.104677.

[32] Ciriello V, Di Federico V, Riva M, Cadini F, De Sanctis J, Zio E, Guadagnini A. Polynomial chaos expansion for global sensitivity analysis applied to a model of radionuclide migration in a randomly heterogeneous aquifer. Stoch Environ Res Risk Assess 2012;27(4):945–54. http://dx.doi.org/10.1007/s00477-012-0616-7.

[33] Ciriello V, Lauriola I, Tartakovsky DM. Distribution-based global sensitivity analysis in hydrology. Water Resour Res 2019;55(11):8708–20. http://dx.doi.org/10.1029/2019wr025844.
[34] Chiofalo A, Ciriello V, Tartakovsky D. Transfer learning of neural surrogates on multifidelity groundwater simulations. Adv Water Resour 2025;206:105140. http://dx.doi.org/10.1016/j.advwatres.2025.105140.
[35] Staedtke H. Gasdynamic aspects of two-phase flow: Hyperbolicity, wave propagation phenomena and related numerical methods. Wiley; 2006.
[36] Span R, Wagner W. A new equation of state for carbon dioxide covering the fluid region from the triple-point temperature to 1100 K at Pressures up to 800 MPa. J Phys Chem Ref Data 1996;25(6):1509–96. http://dx.doi.org/10.1063/1.555991.
[37] Bell IH, Wronski J, Quoilin S, Lemort V. Pure and pseudo-pure fluid thermophysical property evaluation and the open-source thermophysical property library CoolProp. Ind Eng Chem Res 2014;53(6):2498–508. http://dx.doi.org/10.1021/ie4033999.
[38] Huber ML, Sykioti EA, Assael MJ, Perkins RA. Reference correlation of the thermal conductivity of carbon dioxide from the triple point to 1100 K and up to 200 MPa. J Phys Chem Ref Data 2016;45(1):013102. http://dx.doi.org/10.1063/1.4940892.
[39] Laesecke A, Muzny CD. Reference correlation for the viscosity of carbon dioxide. J Phys Chem Ref Data 2017;46(1):013107. http://dx.doi.org/10.1063/1.4977429.
[40] Michelsen ML. State function based flash specifications. Fluid Phase Equilib 1999;158–160:617–26. http://dx.doi.org/10.1016/S0378-3812(99)00092-8.
[41] Benjelloun S, Ghidaglia J-M. On the sound speed in two-fluid mixtures and the implications for CFD model validation. Eur J Mech B Fluids 2021;90:152–68. http://dx.doi.org/10.1016/j.euromechflu.2021.09.002.
[42] Log AM, Hammer M, Deng H, Austegard A, Hafner A, Munkejord ST. Depressurization of CO2 in a pipe: Effect of initial state on non-equilibrium two-phase flow. Int J Multiph Flow 2024;170:104624. http://dx.doi.org/10.1016/j.ijmultiphaseflow.2023.104624.
[43] Wood A. A textbook of sound. G. Bell and Sons; 1941.
[44] Colebrook CF, White CM, Taylor GI. Experiments with fluid friction in roughened pipes. Proc R Soc Lond Ser A - Math Phys Sci 1937;161(906):367–81. http://dx.doi.org/10.1098/rspa.1937.0150.
[45] Dittus F, Boelter L. Heat transfer in automobile radiators of the tubular type. Int Commun Heat Mass Transfer 1985;12(1):3–22. http://dx.doi.org/10.1016/0735-1933(85)90003-X.
[46] Kandlikar SG. A general correlation for saturated two-phase flow boiling heat transfer inside horizontal and vertical tubes. J Heat Transf 1990;112(1):219–28. http://dx.doi.org/10.1115/1.2910348.
[47] Toro E. Centred TVD schemes for hyperbolic conservation laws. IMA J Numer Anal 2000;20(1):47–79. http://dx.doi.org/10.1093/imanum/20.1.47.
[48] Lax PD. Weak solutions of nonlinear hyperbolic equations and their numerical computation. Comm Pure Appl Math 1954;7(1):159–93. http://dx.doi.org/10.1002/cpa.3160070112.
[49] Richtmyer RD, Morton KW. Difference methods for initial-value problems. SAO/NASA Astrophysics Data System; 1967.
[50] Lu C, Michal G, Godbole A, Venton P, Fletcher L. Re-examination of battelle two curve method. In: Volume 3: materials and joining; risk and reliability. Calgary, Alberta, Canada: American Society of Mechanical Engineers; 2014, http://dx.doi.org/10.1115/IPC2014-33143.
[51] Andreasen A, Sousa L-H, Agustsson G. An open source tool for calculating CO2 pipeline decompression wave speed. SNE 2022;32(4):187–93. http://dx.doi.org/10.11128/Sne.32.Tn.10622, 2022.
[52] Oosterkamp A, Ramsen J. State-of-the-art overview of CO2 pipeline transport with relevance to offshore pipelines. Technical report POL-O-2007-138-A, Haugesund, Norway: Polytec R&D Foundation; 2008, Prepared for the Research Council of Norway, Gassco and Shell Technology Norway.
[53] Sudret B. Global sensitivity analysis using polynomial chaos expansions. Reliab Eng Syst Saf 2008;93(7):964–79. http://dx.doi.org/10.1016/j.ress.2007.04.002.
[54] Webster M, Tatang MA, McRae GJ. Application of the probabilistic collocation method for an uncertainty analysis of a simple ocean model. Technical report MIT joint program on the science and policy of global change reports series No. 4, Cambridge, MA: MIT; 1996.
[55] Sobol I. Global sensitivity indices for nonlinear mathematical models and their Monte Carlo estimates. Math Comput Simulation 2001;55(1–3):271–80. http://dx.doi.org/10.1016/s0378-4754(00)00270-6.
[56] Li H, Jakobsen JP, Wilhelmsen Ø, Yan J. PVTxy properties of CO2 mixtures relevant for CO2 capture, transport and storage: Review of available experimental data and theoretical models. Appl Energy 2011;88(11):3567–79. http://dx.doi.org/10.1016/j.apenergy.2011.03.052.
[57] Log AM, Hammer M, Deng H, Austegard A, Munkejord ST. Temperature response during rapid depressurization of CO 2 in a pipe: Experiments and fluid-dynamics modelling. Int J Multiph Flow 2025;192:105330. http://dx.doi.org/10.1016/j.ijmultiphaseflow.2025.105330.
[58] Félix LM, da Fonseca JEF, Kwietniewski CF, Borges MF, Haag J, Dalpiaz G. In: ASME, editor. The effect of nickel on fracture toughness at low temperature for hydrogen pre-charged steel samples. International conference on offshore mechanics and arctic engineering, vol. Volume 5: Materials Technology; Petroleum Technology, 2014, V005T03A007. http://dx.doi.org/10.1115/OMAE2014-23274.
[59] Mahgerefteh H, Denton G, Rykov Y. Pressurised CO2 pipeline rupture. Inst Chem Eng Symp Ser 2008;869–79.
[60] Vitali M, Zuliani C, Corvaro F, Marchetti B, Terenzi A, Tallone F. Risks and safety of CO2 transport via pipeline: A review of risk analysis and modeling approaches for accidental releases. Energies 2021;14(15). http://dx.doi.org/10.3390/en14154601.